Second-order and real Chern topological insulator in twisted bilayer α-graphyne

Bin-Bin Liu [1], Xu-Tao Zeng [1], Cong Chen,[1,2] Ziyu Chen [1,*] and Xian-Lei Sheng [1,3,†]

[1]*School of Physics, Beihang University, Beijing 100191, China*
[2]*Department of Physics, University of Hong Kong, Hong Kong 999077, China*
[3]*Peng Huanwu Collaborative Center for Research and Education, Beihang University, Beijing 100191, China*

The study of higher-order and real topological states as well as the material realization have become a research forefront of topological condensed matter physics in recent years. Twisted bilayer graphene (tbG) is proved to have higher-order and real topology. However, whether this conclusion can be extended to other two-dimensional twisted bilayer carbon materials and the mechanism behind it lack explorations. In this paper, we identify the twisted bilayer α-graphyne (tbGPY) at large twisting angle as a real Chern insulator (also known as Stiefel-Whitney insulator) and a second-order topological insulator. Our first-principles calculations suggest that the tbGPY at 21.78° is stable at 100 K with a larger bulk gap than the tbG. The nontrivial topological indicators, including the real Chern number and a fractional charge, and the localized in-gap corner states are demonstrated from first-principles and tight-binding calculations. Moreover, with $\mathcal{C}_{6z}$ symmetry, we prove the equivalence between the two indicators, and explain the existence of the corner states. To decipher the real and higher-order topology inherited from the moiré heterostructure, we construct an effective four-band tight-binding model capturing the topology and dispersion of the tbGPY at large twisting angle. A topological phase transition to a trivial insulator is demonstrated by breaking the $\mathcal{C}_{2y}$ symmetry of the effective model, which gives insights on the trivialization of the tbGPY as reducing the twisting angle to 9.43° suggested by our first-principles calculations.

I. INTRODUCTION

The discovery of the topological insulator (TI) has stimulated a vibrant research field in condensed matter physics [1–4]. A TI in d dimensions has an insulating bulk, but features topologically protected gapless states on its $(d − 1)$-dimensional (D) boundaries. Recently, the concept was extended to a novel class of topological phase—the higher-order TI [5–10]. An nth-order TI has topological gapless states at its $(d − n)$D boundaries, but is gapped otherwise. For instance, a second-order topological insulator (SOTI) in 2D hosts topological gapless states at its 0D corners between its edges that are gapped. Previous works first reveal the higher-order TIs in 3D materials [10–19]. Then in 2D there are a few material candidates being proposed, such as the graphdiyne family [20–23], twisted bilayer graphene (tbG) [24,25], black phosphorene [26,27], Bi/EuO [28], and monolayer group-V [29,30] and group-IV materials [31,32]. It is still a big challenge to find more realistic 2D SOTI materials.

With the spacetime inversion symmetry, the wave function over the Brillouin zone (BZ) is real instead of complex. The so-called real topology is characterized by the real Berry bundles over the BZ and can be indicated by the real Chern number (RCN) [33] or the second Stiefel-Whitney number [34]. Twisting one layer of the *AA*-stacking periodic lattice structures with translational symmetry, one can obtain a larger supercell which forms the so-called moiré pattern. In the field of twistronics, the tbG is a pioneer material that has been investigated in many aspects including topology. The tbG moiré system is shown to be topological [35] and features a nontrivial RCN or the second Stiefel-Whitney number [24,36]. An insulator with nontrivial RCN (or second Stiefel-Whitney number) like tbG can be referred to as a real Chern insulator (RCI) [37] (or Stiefel-Whitney insulator [22]). Besides, the tbG system at relatively large moiré twisting angle, say 21.78°, is further proved to be a SOTI by explicitly demonstrating the existence of the corner states [24].

By inserting the acetylenic linkage into graphene lattice, many carbon allotropes can be constructed [38,39]. Except for graphene, other 2D carbon allotropes with twisted bilayer structures are lacking of exploration, such as (α, β, γ)-graphyne [39] and graphdiyne [40–43]. These materials with hexagonal lattices all have the same space group symmetry as graphene, but their properties are not identical to graphene and vary in their own way due to the presence of the acetylenic linkage [44]. So their twisted bilayer structures do not necessarily behave like the tbG.

Among these graphynes, the α-graphyne is the most similar one to graphene. As studied in Refs. [39,45–47], α-graphyne has eight carbon atoms per unit cell [see Fig. 1(a)], which can be regarded as inserting an acetylenic linkage between every two atoms in graphene. The symmetry group for α-graphyne (and graphene) is the No. 191 space group with point group D_{6h} ($p6m$ symmetry). The α-graphyne shares some properties with graphene. For example, the band structure of the α-graphyne features a similar linear gapless cone at

*chenzy@buaa.edu.cn
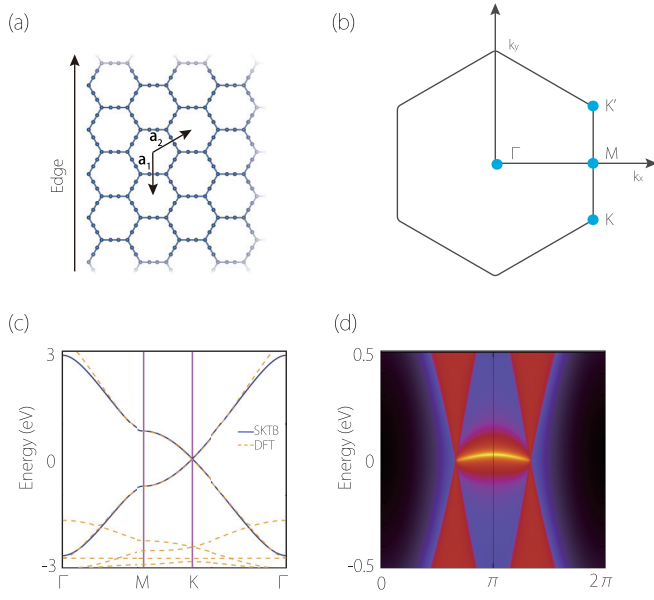†xlsheng@buaa.edu.cn

035153-1

FIG. 1. (a) Crystal structure and unit cell of the α-graphyne with a zigzag edge. (b) shows the high-symmetry points in the first Brillouin zone used in our calculations. (c) and (d) show the bulk and edge band structures for the monolayer α-graphyne.

the K in the BZ as shown in Fig. 1(c). Therefore, it is natural to ask whether the twisted bilayer α-graphyne (tbGPY for short) can inherit the second-order and real topology from the moiré heterostructure like the tbG at large twisting angle.

In this paper, we address the issue by exploring the electronic and topological properties of the tbGPY. Based on tight-binding and first-principles calculations, we identified the tbGPY at large twisting angle as a RCI and a SOTI, which has a larger bulk gap than the tbG. We confirmed the bulk topology from both the nontrivial RCN ν_R [23,33] and a fractional charge $Q^{(2)}_{\text{corner}}$ [48] that indicates a filling anomaly. With the $\mathcal{C}_{6z}$ symmetry, we strictly proved that the nontrivial RCN equals an $e/2$ fractional charge $Q^{(2)}_{\text{corner}}$, which in turn suggests the existence of corner states on a hexagonal lattice. We further calculated the energy level of a hexagonal nanodisk for the tbGPY at $21.78°$ and found six in-gap localized corner states, which exemplifies the bulk-boundary correspondence of a RCI with $\mathcal{C}_{6z}$ symmetry. The robustness of the corner states against symmetry-breaking disorders was demonstrated. We also performed an *ab initio* molecular dynamics calculation which suggests that the tbGPY at $21.78°$ is stable at 100 K.

Moreover, we built an effective tight-binding model to decipher the SOTI and RCI state inherited from the moiré heterostructure of tbGPY. The model features a RCI as well as a SOTI with nontrivial fractional charge, and can be transited to a trivial insulator by breaking $\mathcal{C}_{2y}$ symmetry. To extend, the model can be applied to other twisted bilayer materials with a Dirac cone at the K point in the monolayer, such as the tbG. Different from the tbG, we observed that the RCI state in tbGPY becomes trivial as the twisting angle becomes smaller. This trivialization can be simulated by our effective model through the topological phase transition.
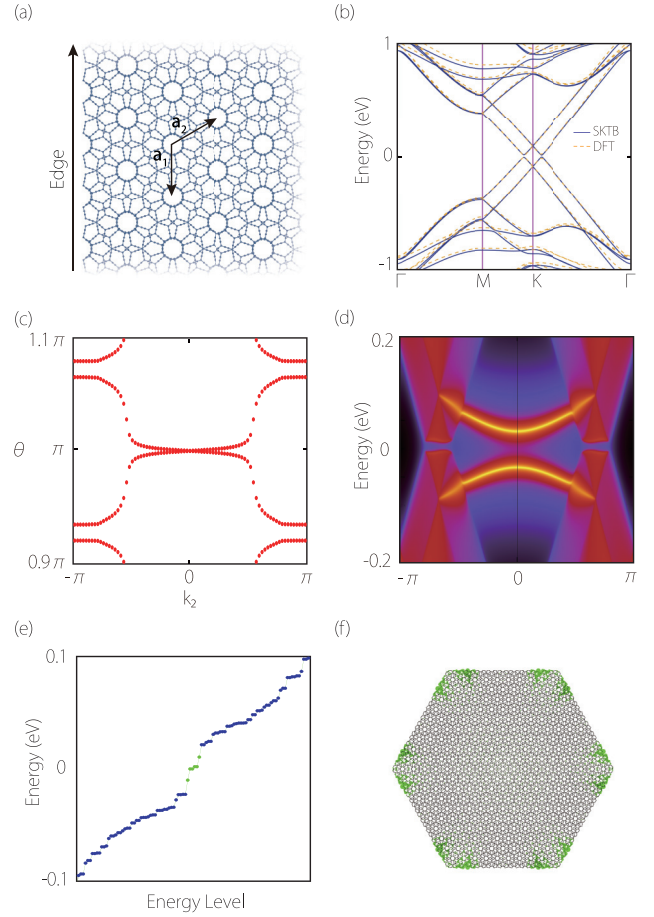

FIG. 2. The tbGPY ($i = 1$) material and its properties. (a) Crystal structure with lattice vectors and a specified armchair edge. (b) and (d) show the gapped bulk and edge spectra with a gap around 13 meV for the bulk and 65 meV for the edge. (c) The Wilson loop spectrum around $\theta = \pi$, which indicates the nontrivial RCN ($\nu_R = 1$). (e) The energy levels of the hexagonal nanodisk in (f) near the Fermi level. (f) The real-space distribution of the six in-gap states marked as green dots in (e), suggesting the localized corner states.

II. LATTICE AND BAND STRUCTURES

We begin by introducing the general geometry for the twisted bilayer moiré system with a hexagonal lattice. To obtain the moiré pattern, one may stack two periodic lattice planes together (i.e., *AA* stacking), and then twist one layer with respect to the other with respect to a certain commensurate angle. For the hexagonal lattice unit cell, the commensurate angle can be formulated as $\theta_i = \arccos(\frac{3i^2+3i+0.5}{3i^2+3i+1})$ (where i is an integer above zero) [49]. The commensurate condition does not depend on the inversion center, and is chosen as the middle of the hexagon lattice [Fig. 1(a)] in this work. The moiré pattern and the associated lattice vectors only depend on the twisting angle or the index i. In the following, we use the i to label the commensurate angle.

The lattice structure of the twisted bilayer α-graphyne at the commensurate angle $21.78°$ with $i = 1$ is shown in Fig. 2(a), which is the main focus of the paper. To test the dynamical stability, we performed a molecular dynamics

simulation for the tbGPY and find that it is dynamically stable under at least 100 K. The simulation result is summarized in Appendix A. Its moiré supercell contains 112 carbon atoms, seven times as large as the *AA*-stacking α-graphyne. We obtained the layer distance of the tbGPY with a first-principles relaxation calculation, which is $d_0 = 3.444$ Å, in agreement with previous studies [50]. See Appendix B 1 for calculation details. Different from the monolayer α-graphyne, the tbGPY lies in the No. 177 space group with D_6 point group symmetry. The generators for this associated point group can be chosen as $\mathcal{C}_{6z}$ and $\mathcal{C}_{2y}$.

We calculated the energy dispersion of the tbGPY with $i = 1$ based on density functional theory. The result is shown in the dashed lines in the Fig. 2(b), which is calculated along the line connecting the high-symmetry points specified in Fig. 1(b). We found a sizable gap of around 12.8 meV. To compare, we also calculate the energy spectrum for the twisted bilayer graphene with layer distance 3.35 Å using the same calculation method, and find a gap of around 1.4 meV at K. See Appendix B 1 for explanations of the method. The opening of the band gap for the tbGPY can be understood from the $U_v(1)$ valley symmetry breaking for the bulk cones.

To proceed, we constructed a symmetry-based tight-binding model with the method introduced by Slater and Koster [51]. The details for the method are shown in Appendix B 2. Following the method, we constructed a Slater-Koster tight-binding (SKTB) model for tbGPY with one p_z orbital per site. The fitted energy dispersion for the tbGPY using the SKTB model is shown in Fig. 2(b) with solid lines, which captures the main feature of the energy dispersion of tbGPY in the low-energy range.

The parameters for the SKTB model are illustrated as follows. The SKTB model includes all the couplings that have bond lengths less than the range of $L = 5$ Å. The nearest-neighbor distance in the monolayer α-graphyne is $a_0 = 1.232$ Å, and the layer distance of the tbGPY is $d_0 = 3.444$ Å. The nearest-neighbor p-p π coupling is fitted as $V_{pp\pi}^0 = -4.45$ eV while the nearest p-p σ coupling is $V_{pp\pi}^0 = 0.32$ eV. Other orbital couplings are determined relatively to those nearest ones by their relative distance to a_0 and d_0 [see Eq. (B3) and Eq. (B4)]. The decay length of the transfer integral is chosen as $\delta_0 = 0.32$ Å. The on-site energy for each orbital is fitted as -0.156 eV. In the following, we investigate the topological properties of the material.

III. REAL CHERN NUMBER

For a spinless system, under the spacetime inversion symmetry $\mathcal{PT}$, the wave function over the BZ is real instead of complex. In such case, the topology is characterized by the real Berry bundles over the BZ and can be termed as the real topology. The topological indicator for the real topology is the the RCN [33], or the second Stiefel-Whitney number [34]. The RCN is the defining topological invariant for the RCI as well as other exotic topological phases such as the second-order nodal-line semimetal [37,52]. In 2D the defining spacetime inversion symmetry $\mathcal{PT}$ can be replaced with the $\mathcal{C}_{2z}\mathcal{T}$ symmetry. Originated from the D_6 point group, the tbGPY has the $\mathcal{C}_{2z}$ symmetry, while also possessing the

TABLE I. The RCNs and fractional charges for tbGPY material and effective 4BTB model. The first two columns indicate the systems with different i. The remaining columns are the RCN ν_R and the fractional charge of $Q_{corner}^{(2)}$ calculated by Eqs. (2) and (3). The first two rows are tbGPY with $i = 1$ calculated from first principles and simulated by the topological 4BTB model. The last two rows are the tbGPY with $i = 3$ calculated from first principles and simulated by the trivial 4BTB model (which differs from the topological 4BTB model in $t_b = -t_t = -1/3$ eV).

i	System	ν_R	$Q_{corner}^{(2)}$
$i = 1$	tbGPY	1	$e/2$
	Topological 4BTB	1	$e/2$
$i = 3$	tbGPY	0	0
	Trivial 4BTB	0	0

time-reversal symmetry $\mathcal{T}$. So it has the combined symmetry $\mathcal{C}_{2z}\mathcal{T}$ required for the real topological classification.

In practice, there are two ways to compute the RCN [23]. One is the well-known Wilson loop method: calculating the Wilson loop along a chosen direction, e.g., $\mathbf{k}_1$, with fixed $k_2 \in [-\pi, \pi)$. This results in N (the number of valence bands of the system) curves in the k_2-θ diagram, which represents the evolution of the Wannier center. The parity of the winding number or equivalently the RCN (ν_R) can be read off from the times of crossings (ζ) of the Wilson loop spectrum with the $\theta = \pi$ line [53], i.e.,

$$\nu_R = \zeta \bmod 2. \tag{1}$$

When not only the $\mathcal{PT}$ but also the $\mathcal{P}$ symmetry is preserved, there is another more intuitive method to calculate the RCN, which is by counting the parity eigenvalues of the valence bands at the four time reversal invariant momenta (TRIM) points Γ_i. Practically, one may follow

$$(-1)^{\nu_R} = \prod_{i=1}^{4} (-1)^{\lfloor (n_-^{\Gamma_i}/2) \rfloor}, \tag{2}$$

to compute the RCN ν_R, where the $n_-^{\Gamma_i}$ is the number of the minus parity in the valence band at Γ_i.

We calculated the RCN for tbGPY with both methods. With the fist method, we obtained the Wilson loop from the SKTB model of tbGPY as in Fig. 2(c), where a single crossing of the spectrum with π suggests the RCN to be nontrivial, i.e., $\nu_R = 1$. With the second parity counting method, we calculate the parity eigenvalues of the $\mathcal{C}_{2z}$ at TRIM points from first-principles calculations. Using Eq. (2), the RCN is also found to be nontrivial. The parity counting method can be further simplified in our case. As the tbGPY lattice possesses the $\mathcal{C}_{6z}$ symmetry, three of the TRIM points (*M* points) are equivalent, so that we only need to calculate one *M* point instead all three of them. Detailed information about the RCN calculation is shown in Table II in Appendix D. Our results suggests that the tbGPY system is a RCI at large commensurate angle.

The second parity counting method is more physically intuitive, because it tells us information about band inversion. For example, a nontrivial RCN in Table II corresponds to a double band inversion at the Γ point.

TABLE II. The RCNs for tbGPY systems with $i = 1$–4 calculated from first principles. The first two columns are the commensurate twisting angles and their labels; the third column is the number of valence band for first-principles calculations. The fourth and fifth columns are the number of minus parity at the Γ and M counted from the valence bands. The last column suggests the RCNs calculated from the fourth and fifth columns using Eq. (2).

i	Twisted angle (deg)	Number of valence bands	n_-^Γ	n_-^M	RCN
1	21.787	224	110	112	1
2	13.174	608	302	304	1
3	9.430	1184	592	592	0
4	7.341	1952	976	976	0

A nontrivial RCN in a $\mathcal{PT}$-invariant system could feature a rich boundary correspondence [37]. This means that despite having a nontrivial RCN, the tbGPY is not necessarily a SOTI. In the following, we explore the bulk-boundary correspondence for the tbGPY system and prove that it is a SOTI with nontrivial fractional charge that features localized corner states in a hexagonal lattice.

IV. BULK-BOUNDARY CORRESPONDENCE

In 2D, a TI has topologically protected gapless edge states, while for a SOTI the edge state is gapped but the conducting corner charges in the edge gap emerge. To proceed, we first calculate the edge spectrum for the tbGPY ($i = 1$) and compare it with that of monolayer graphyne. In Fig. 2(d) and Fig. 1(d), we show the edge spectra for the tbGPY and the monolayer α-graphyne with the edges illustrated in the Fig. 2(a) and Fig. 1(a). Comparing the two, we find that instead of trivially stacking, the two bulk Dirac cones in tbGPY are shifted to higher and lower energies with a gap in between. Correspondingly, the edge states (bright yellow curves) that are associated with the bulk Dirac cones are also shifted upward and downward, resulting in an edge gap. The edge gap is found to be around 65 meV which is larger than the bulk gap of 13 meV [Fig. 2(d)].

Then we explore the property of the second-order boundaries (corners) of tbGPY on a hexagonal nanodisk geometry related by $\mathcal{C}_{6z}$ rotation symmetry. Inside the edge gap, we find six localized corner states in the nanodisk. Specifically, we calculate the energy level of a hexagonal nanodisk of tbGPY with 33 360 carbon atoms (p_z orbitals), and find six states inside the edge gap marked as green dots, as shown in Fig. 2(e). The observed nondegeneracy of the energy levels of the six corner states is due to the slight breaking of chiral symmetry in the tbGPY and the size effect of the nanodisk. This is proved in our effective model analysis. We plot the charge distribution of the six in-gap states and find that they are localized at six corners of the hexagonal nanodisk in Fig. 2(f).

We now briefly introduce the concept of fractional charge to explain the presence of the six corner states. The fractional charge is a bulk property that indicates the filling anomaly of electrons and is defined under crystalline symmetries. Under the $\mathcal{C}_{2z}$, a fractional charge termed $Q_{\text{corner}}^{(2)}$ can be defined [48] (see Appendix C for details). Further considering $\mathcal{C}_{6z}$ symmetry as in the tbGPY case, we can relate the $Q_{\text{corner}}^{(2)}$ with the RCN in a neat form,

$$Q_{\text{corner}}^{(2)} = e \frac{\nu_R}{2}. \tag{3}$$

According to Ref. [48], the fractional charge is a secondary indicator which is well defined with the vanishing of the polarization indicator $\mathbf{P}^{(2)}$. Remarkably, under the protection of $\mathcal{C}_{6z}$ symmetry, we find

$$\mathbf{P}^{(2)} = \mathbf{0}. \tag{4}$$

This is illuminating since it indicates a correspondence between the RCI and a SOTI with localized corner states. A nontrivial RCN is a bulk property, which in the presence of $\mathcal{C}_{6z}$ is equivalent to a nontrivial well-defined fractional charge $Q_{\text{corner}}^{(2)}$ that corresponds to secondary boundary states related by $\mathcal{C}_{2z}$. Here we derive the correspondence [Eq. (3) and Eq. (4)] with $\mathcal{C}_{6z}$; therefore there can exist six localized corner states in general. We further demonstrate that the tbGPY ($i = 1$) owns nontrivial fractional charges of $Q_{\text{corner}}^{(2)} = e/2$ through first principles. Therefore, the hexagonal nanodisk of tbGPY hosts six corner states, as shown in Fig. 2(f) and in Fig. 3(f) in Sec. V B.

The six corner charges are robust against disorders along the edge, provided that the bulk and edge energy gaps remain open. This is because the disorder might shift the in-gap corner charges by only an integer, but leaves the fractional part intact. The detailed calculations and discussions for the tbGPY nanodisk with disorder can be found in Fig. 5 and in Appendix C.

We have demonstrated the bulk-boundary correspondence of the tbGPY ($i = 1$) by showing that it is not only a RCI, but also a SOTI with localized in-gap corner states.

V. EFFECTIVE FOUR-BAND MODEL

To decipher the higher-order and real topology inherited from the complex moiré supercell of tbGPY with numerous atoms, we provide a simpler effective model with only four orbitals that captures the nontrivial topological properties.

A. Model construction

We build the effective TB model starting from the symmetries of tbGPY. By effective, we mean that the effective model captures the main features of the bulk and edge dispersions, possesses the nontrivial topology, i.e., the nontrivial RCN and fractional charge, and characterizes the localized corner states.

To achieve the requirement, we find the symmetries for constructing the effective model can be $\mathcal{C}_{2z}\mathcal{T}$ and crystalline $\mathcal{C}_{6z}$ and $\mathcal{C}_{2y}$. Due to the presence of the combined $\mathcal{C}_{2z}\mathcal{T}$ that defines the real topology, there exists a Wannier obstruction for building a two-band tight-binding model [36,54]. Following the strategy in Refs. [35,54], we build a four-band
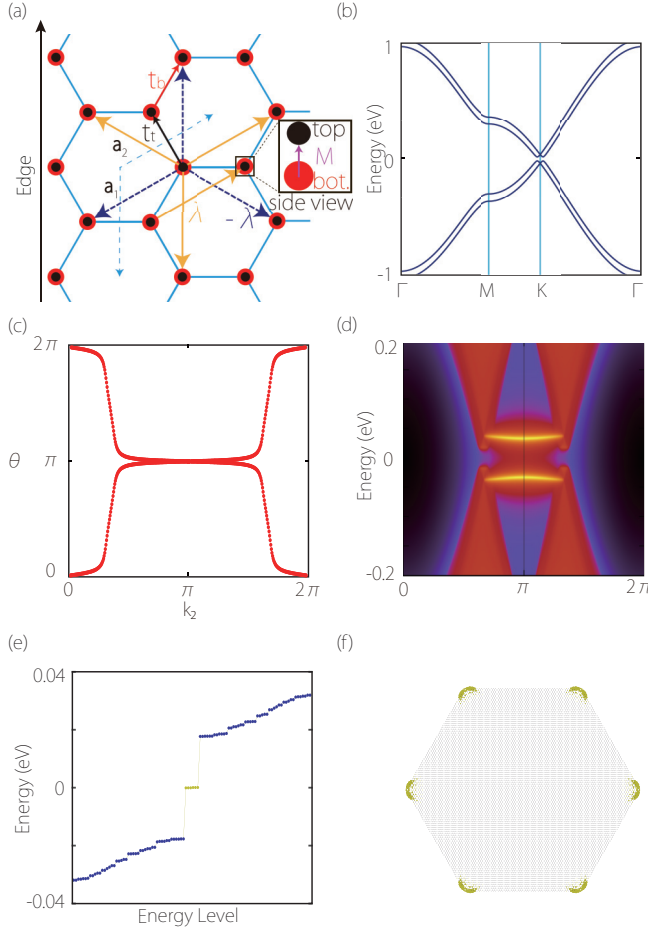
FIG. 3. The topological 4BTB model and its properties. (a) Lattice, orbitals, and specified hoppings with a zigzag edge. (b) and (d) show the gapped bulk and edge band structures. (c) The Wilson loop spectrum indicating the nontrivial RCN, $\nu_R = 1$. (e) The energy levels of the hexagonal nanodisk in (f). (f) The charge distribution of the six in-gap states (marked as green dots) in (e), indicating the presence of the localized corner states. The parameters are chosen as $t_t = t_b = t = 1/3$ eV, $\lambda = 0.01t$, and $M = 0.1t$ for calculation.

tight-binding (4BTB) model in a honeycomb lattice, as shown in Fig. 3(a). The four orbitals of our 4BTB model form two layers with each layer two sublattices in a unit cell. Here, we do not distinguish the orbital type, i.e., whether they are
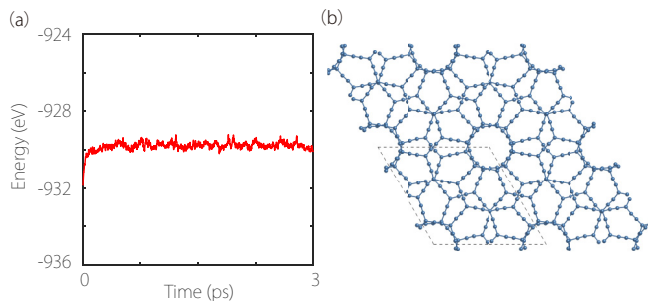

FIG. 4. AIMD simulation results for tbGPY ($i = 1$). (a) Variation of the total energy during the AIMD simulation at 100 K. (b) Lattice structure at the end of the simulation period.
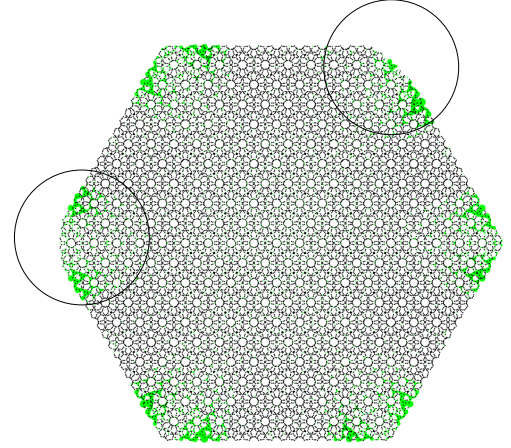

FIG. 5. Robustness of corner states on a disordered hexagonal nanodisk of tbGPY $i = 1$. The disorders are introduced at the corners enclosed by circles.

s or p_z orbitals. Without loss of generality, one may assume four s orbitals with each orbital per site. Incorporating the symmetries into the orbitals, we can immediately specify the hoppings for the model as shown in Fig. 3(a).

Now we explain the coupling bonds for the 4BTB model. The black and red arrows are the nearest-neighbor hoppings for the top and bottom layers, which generate two degenerated copies of massless Dirac cones at the K point as that of graphene. The amplitudes of the hoppings are denoted as t_t (top) and t_b (bottom). The pink bond (denoted as M) connects each of the nearest top and bottom orbitals as shown in the side view in Fig. 3(a). This bond functions as the energy shifting term which shifts the two Dirac cones upward and downward, which guarantees a gap for the edge spectrum. To have a bulk band gap around K, we introduce the alternative hoppings λ that connect the top and bottom layer orbitals with solid orange and dashed dark blue arrows. The alternating pattern of the λ is that the sign of the bond changes between positive and negative when rotating $60°$. These terms effectively introduce a gap in the bulk, corresponding to the moiré twisting in tbGPY. The 4BTB model in momentum space then reads

$$H^{4\text{BTB}}(\mathbf{k}) = \begin{bmatrix} G_t & M\sigma_0 + iS \\ M\sigma_0 - iS & G_b \end{bmatrix} \quad (5)$$

with

$$G_j = t_j \sum_{i=1}^{3} [\sigma_x \cos(\boldsymbol{\delta}_i \cdot \mathbf{k}) - \sigma_y \sin(\boldsymbol{\delta}_i \cdot \mathbf{k})] \quad (j = t, b),$$

$$S = 2\lambda\sigma_z \sum_{i=1}^{3} \sin(\mathbf{d}_i \cdot \mathbf{k}).$$

The σ_0 is a 2×2 identity matrix, and the $\sigma_{x,y,z}$ are Pauli matrices acting on the sublattice degrees of freedom. The Hamiltonian in Eq. (5) distinguishes top and bottom layers. The $\boldsymbol{\delta}_1 = \frac{1}{3}\mathbf{a}_1 + \frac{2}{3}\mathbf{a}_2$, $\boldsymbol{\delta}_2 = -\frac{2}{3}\mathbf{a}_1 - \frac{1}{3}\mathbf{a}_2$, and $\boldsymbol{\delta}_3 = \frac{1}{3}\mathbf{a}_1 - \frac{1}{3}\mathbf{a}_2$ are the nearest hopping vectors within one layer, while $\mathbf{d}_1 = \mathbf{a}_1$, $\mathbf{d}_2 = \mathbf{a}_2$, and $\mathbf{d}_3 = -\mathbf{a}_1 - \mathbf{a}_2$ are the second-nearest hopping vectors within one layer. Note that the hopping

parameters of the 4BTB model are all real numbers due to an emergent $\mathcal{T}$ symmetry. Therefore the 4BTB model recovers the same symmetries as tbGPY.

B. Nontrivial bulk-boundary correspondence

To examine the validity of the effective 4BTB model, we check the criterion mentioned at the beginning of the Sec. V A. Specifically, we set $t_t = t_b = t = 1/3$ eV, $\lambda = 0.01t$, and $M = 0.1t$ for the model. The parameters are obtained by simulating the main features of the bulk band of tbGPY around K.

The bulk property concerns band dispersion as well as the topological indicators. The band structure has a small gap around K with a valley splitting feature, in agreement with the material calculations of tbGPY, as shown in Fig. 3(b) and Fig. 2(b). The RCN as well as the fractional charges $Q_{\text{corner}}^{(2)}$ are all nontrivial and agree with the tbGPY ($i = 1$) as shown in the $i = 1$ row of Table I. We also calculate the RCN with the Wilson loop technique. We calculate the Wannier center evolution along the k_2 which has two curves and a single crossing point at $\theta = \pi$, which means the RCN is nontrivial. See Fig. 3(c). Therefore, the topological 4BTB model features a RCI with nontrivial fractional charges.

Then we check the boundary correspondence of the topological 4BTB model. We investigate the edge spectrum along the zigzag direction specified in Fig. 3(a), and the result is shown in Fig. 3(d). One observes that each edge connects two bulk cones, and leaves an edge gap in between, which has the same feature as that in Fig. 2(d). To investigate the second-order edge, we construct a nanodisk containing 30 000 orbitals for the 4BTB model. There are six degenerated zero modes at the Fermi level labeled by green dots, as shown in Fig. 3(e), which are distributed at the six corners of the nanodisk as shown in Fig. 3(f). In the model calculation, we are able to eliminate the size effect and hence the corner modes are nearly degenerated at 0 eV. See Appendix E for an explanation of topological origin of the corner state with domain wall theory.

Therefore, we have constructed an effective model with only four orbitals for the tbGPY at large commensurate angle. To extend, the 4BTB model may also be applied to study other twisted bilayer system at large commensurate angle, such as tbG which has the same symmetry as tbGPY and has a Dirac cone at K in the monolayer [24].

C. Topological phase transition

After demonstrating the nontrivial topology of the 4BTB model, it is natural to explore the other side of the model, namely a trivial insulator. We here provide a simple and intuitive way to trivialize the effective 4BTB model. To achieve so, we simply reverse the sign of t_b, following that $t_b = -t_t = -t$. In this way, we break the $\mathcal{C}_{2y}$ symmetry of the 4BTB model and achieve a band inversion between the valence and conductance bands. Since the $\mathcal{C}_{6z}$ symmetry still remains in the model, we can use Eq. (2) and Eq. (3) to calculate the RCN and the fractional charge. The topological indicators for the trivial 4BTB model are both 0 as shown in Table I. Slight breaking of the $\mathcal{C}_{2y}$ symmetry will not spoil the topological

corner states as long as the bulk and edge gaps are not closed [20]. However, here the $\mathcal{C}_{2y}$ symmetry breaking is accompanied with a band inversion, which is the reason that the RCN and the fractional charge become trivial. As a consequence, there is no localized corner state in the trivial 4BTB model, in contrast to that of the topological 4BTB model as shown in Figs. 3(e) and 3(f).

For tbGPY with smaller commensurate angel, say 9.4° with $i = 3$, the RCN becomes trivial (see Appendix D for some details and discussions). This indicates a band inversion. The trivial 4BTB model features the same RCN and fractional charge as the material with $i = 3$ as presented in Table I, and gives an understanding of the trivialization process from the symmetry-breaking and band-inversion prospects.

VI. CONCLUSION AND OUTLOOK

In conclusion, we proposed the tbGPY at large commensurate angle as a RCI and a SOTI from first-principles and tight-binding model calculations. The tbGPY has a sizable bulk gap of around 13 meV larger than the tbG and is stable at 100 K, which is favorable for the experimental detection of the corner states. To decipher the topological property inherited from the moiré structure, we constructed a simple but effective 4BTB model which captures the major topological features of the tbGPY. The model may also apply to other twisted bilayer systems with a Dirac cone at K in the monolayer, such as the tbG. A phase transition of the effective model by breaking the $\mathcal{C}_{2y}$ symmetry is also studied, which gives insights on the trivialization of the RCI state in the tbGPY. Moreover, in the presence of $\mathcal{C}_{6z}$ symmetry, we prove that the nontrivial RCN ν_R equals an $e/2$ fractional charge $Q_{\text{corner}}^{(2)}$, which in turn explains the six localized corner states in the tbGPY hexagonal nanodisk.

We give an outlook on the experimental realization of the RCI and SOTI in artificial systems with the 4BTB model. In the topological 4BTB model, all the hopping amplitudes are real, either positive or negative, which preserves the time-reversal symmetry $\mathcal{T}$. Therefore, the model can be realized in a rich category of artificial systems, such as electrical circuit systems [55], phonon lattices [56–58], photonic crystals [59,60], mechanical systems [61], and cold atoms [62]. Moreover, a topological phase transition can be realized by simply reversing the sign of the nearest-neighbor hoppings in the bottom/top layer $t_{b/t}$, which can be engineered to tune the existence of the corner states. In addition, removing the M term in the 4BTB model, the remaining spinless model with pseudospin generated by the layer operator τ behaves effectively like the spinful model by Kane and Mele [63]. Here the model can be realized with real hopping amplitudes and without spin degree which is favorable for realizations in artificial systems.

APPENDIX A: MOLECULAR DYNAMICS STUDY OF THE tbGPY

To assess the dynamical stability of the tbGPY, we performed an *ab initio* molecular dynamics (AIMD) simulation at 100 K. With a time step of 1.5 fs, for total 3 ps. We find the variation of the total energy is small, and the structure of tbGPY and the moiré pattern do not change much after the simulation, as shown in Fig. 4. Therefore, we can conclude that there are no obvious distortions of the geometries for tbGPY heterostructure at 100 K, which suggests that it is dynamically stable at 100 K.

APPENDIX B: METHODS

1. First-principles calculation

Our first-principles calculation is carried out based on the density functional theory implemented in the Vienna *ab initio* simulation package (VASP) [64,65]. The projector augmented wave (PAW) method [66] was used for treating the ionic potentials. The generalized gradient approximation (GGA) with the Perdew-Burke-Ernzerhof (PBE) [67] realization was adopted for the exchange-correlation functional. The plane-wave cutoff energy was set to 520 eV. Only the Γ point is chosen for the BZ sampling in the self-consistent calculations, considering the large unit cell of the moiré structure. A vacuum of around 20 Å is included in the simulation to reduce the unwanted interaction between any graphyne bilayers. The crystal structure optimization is stopped when the forces on the ions are less than 0.01 eV/Å. The energy convergence criteria is set as 10^{-6} eV for the electronic self-consistent calculations. The van der Waals corrections are carried out in the relaxation calculations by the semiempirical density functional theory (DFT) D3 method [68] with Becke-Johnson damping [69].

To obtain the layer distance of tbGPY, we performed several full-atom structural relaxations with different initial interlayer distances ranging from 3.664 Å to 2.964 Å with an interval of 0.1 Å. The free energy after relaxation reaches a minimum of -938.3827 eV with the corresponding layer distance of 3.444 Å, as presented in the main text.

2. SKTB model

We study the edge spectra and corner states using the SKTB model, following the Slater and Koster scheme [51,70]. We build the SKTB model with the p_z orbital of the carbon atom in tbGPY. The general Hamiltonian of the SKTB model is written as

$$H = -\sum_{|\mathbf{r}_i - \mathbf{r}_j| < L} h(\mathbf{r}_i - \mathbf{r}_j)|\mathbf{r}_i\rangle\langle\mathbf{r}_j| + \text{H.c.}, \qquad (B1)$$

where $\mathbf{r}_i$ is the position of the lattice point i, and $|\mathbf{r}_i\rangle$ represents the atomic state at site i. The L is the maximum length for the hopping considered. The $h(\mathbf{r}_i - \mathbf{r}_j)$ is the hopping amplitude (transfer integral) between site i and j, which can be calculated using

$$-h(\mathbf{d}) = V_{pp\pi}\left[1 - \left(\frac{\mathbf{d}\cdot\hat{\mathbf{e}}_z}{d}\right)^2\right] + V_{pp\sigma}\left(\frac{\mathbf{d}\cdot\hat{\mathbf{e}}_z}{d}\right)^2, \qquad (B2)$$

with

$$V_{pp\pi} = V_{pp\pi}^0 \exp\left(-\frac{d - a_0}{\delta_0}\right), \qquad (B3)$$

$$V_{pp\sigma} = V_{pp\sigma}^0 \exp\left(-\frac{d - d_0}{\delta_0}\right), \qquad (B4)$$

where the $V_{pp\pi}^0$ is the nearest-neighbor p-p π coupling, and $V_{pp\sigma}^0$ is the nearest-neighbor p-p σ coupling. The nearest distance in the monolayer is a_0, and the layer distance is d_0. To consider the interlayer effect, $L > d_0$ should be satisfied.

APPENDIX C: FRACTIONAL CHARGES AND ROBUSTNESS OF CORNER STATES AGAINST SYMMETRY-BREAKING DISORDERS

The fractional charge quantization of corner states is due to the filling anomaly between the number of electrons required to satisfy the charge neutrality and the crystalline symmetry. The tbGPY preserves $\mathcal{C}_{2z}$ and $\mathcal{C}_{6z}$ symmetries which correspond to fractional charges of $Q_{\text{corner}}^{(2)}$ and $Q_{\text{corner}}^{(6)}$ defined as [48]

$$Q_{\text{corner}}^{(2)} = \frac{e}{4}\left[-n_{C_2}^X - n_{C_2}^Y + \left(n_{C_2}^M + n_{C_2}^\Gamma\right)\right] \bmod e, \qquad (C1)$$

$$Q_{\text{corner}}^{(6)} = e\left(\frac{n_{C_2}^M - n_{C_2}^\Gamma}{4} + \frac{n_{C_3}^K - n_{C_3}^\Gamma}{6}\right) \bmod e, \qquad (C2)$$

where the $n_{C_k}^i$ denotes the number of eigenvalue 1 of $\hat{C}_k$ (alone $\hat{z}$) at the point i in the momentum space. In the presence of $\mathcal{C}_{6z}$ symmetry, the $Q_{\text{corner}}^{(2)}$ admits a more intuitive form shown in Eq. (3) with Eq. (4). As a result, the nontrivial RCN which is a bulk property corresponds to the fractional charge $Q_{\text{corner}}^{(2)} = e/2$ that features a unique boundary property. However, the $Q_{\text{corner}}^{(6)}$ does not give a one-to-one correspondence to the RCN,

$$Q_{\text{corner}}^{(6)} = e\left(\frac{\text{sgn}(n_{C_2}^M - n_{C_2}^\Gamma)\nu_R}{2} + \frac{n_{C_3}^K - n_{C_3}^\Gamma}{6}\right) \bmod e. \quad (C3)$$

We find $Q_{\text{corner}}^{(6)} = e/6$ for the nontrivial tbGPY.

Then we explain this robustness from the point of view of fractional charge. In higher-order topological insulator materials with disorders, if the crystalline symmetry, e.g., the $\mathcal{C}_{2z}$ or $\mathcal{C}_{6z}$, is slightly broken (which does not invert bands), it may cause a ground state filling of the in-gap states. This could shift the corner charges by only an integer, and therefore the fractional portion of the charge remains intact at each corners. We demonstrated the above analysis of the robustness of the corner state by introducing disorders along the edge. Specifically, we removed several atoms at the corners (outlined in Fig. 5) of the hexagonal nanodisk. The disorder breaks the local $\mathcal{C}_{2z}$, $\mathcal{C}_{6z}$, and the $\mathcal{C}_{2y}$ crystalline symmetries in the nanodisk, but does not spoil the corner charges.

APPENDIX D: RCN CALCULATIONS FOR tbGPY AND tbG WITH DIFFERENT TWISTING ANGLES

Using Eq. (2) in the main text with DFT, we calculate the RCNs for tbGPY and tbG, which are presented in Tables II and III. We find a trivialization of RCN in the tbGPY with $i = 3$ and 4. For the tbG systems, however, we have not observed such trivialization of RCN up to $i = 10$.

TABLE III. The RCNs for tbG systems with several $i = 1$–10 calculated from DFT. The arrangement of the table is the same as Table II.

i	Twisted angle (deg)	Number of valence bands	n_-^Γ	n_-^M	RCN
1	21.787	56	24	30	1
2	13.174	152	72	78	1
3	9.430	296	144	150	1
4	7.341	488	240	246	1
5	6.009	728	360	366	1
6	5.086	1016	504	510	1
7	4.409	1352	672	678	1
8	3.890	1736	864	870	1
9	3.481	2168	1080	1086	1
10	3.150	2648	1320	1326	1

Now we discuss briefly the trivialization of the RCN in tbGPY with $i = 3$. Despite the similarities between graphene and α-graphyne, the existence of the acetylenic linkage makes some differences in the α-graphyne. For instance, the acetylenic linkage in the α-graphyne inverts the energy band, which in turn reverses the chirality between the graphene and the α-graphyne at K (or K') [44,45]. The trivialization in the RCN for tbGPY clearly indicates a double band inversion as reducing the twisting angle, while for graphene, such band inversion does not happen down to at least $3.15°$. This difference may be due to the existence of the acetylenic linkage in the α-graphyne.

APPENDIX E: HIGHER-ORDER TOPOLOGICAL ORIGIN FROM DOMAIN WALL THEORY

The existence of corner states can also be understood in light of the domain wall theory. Previous studies [20,23,28,71] suggest that a general SOTI system has the edge of the form

$$H_{edge}(k) = vk\sigma_z + m\sigma_x. \tag{E1}$$

If the mass term is odd under a reflection symmetry which connects two edges, then there should appear a domain wall state at the corner of the two edges. In the 4BTB model the π rotation about the y axis represented as $\mathcal{C}_{2y} = \tau_x\sigma_x$ can serve as the reflection. Under $\mathcal{C}_{2y}$, the velocity term reverses its sign with the mass term unchanged. Therefore, it suggests that the mass term is odd under the $\mathcal{C}_{2y}$, meaning that a domain wall state should appear at the corner where the two edges connected by the $\mathcal{C}_{2y}$ cross. Further considering the $\mathcal{C}_{3z}$ symmetry, there exist six corner states in the hexagonal nanodisk.

[1] M. Z. Hasan and C. L. Kane, Rev. Mod. Phys. **82**, 3045 (2010).
[2] X.-L. Qi and S.-C. Zhang, Rev. Mod. Phys. **83**, 1057 (2011).
[3] S.-Q. Shen, *Topological Insulators* (Springer, Berlin, 2012).
[4] A. Bansil, H. Lin, and T. Das, Rev. Mod. Phys. **88**, 021004 (2016).
[5] F. Zhang, C. L. Kane, and E. J. Mele, Phys. Rev. Lett. **110**, 046404 (2013).
[6] W. A. Benalcazar, B. A. Bernevig, and T. L. Hughes, Science **357**, 61 (2017).
[7] J. Langbehn, Y. Peng, L. Trifunovic, F. von Oppen, and P. W. Brouwer, Phys. Rev. Lett. **119**, 246401 (2017).
[8] Z. Song, Z. Fang, and C. Fang, Phys. Rev. Lett. **119**, 246402 (2017).
[9] W. A. Benalcazar, B. A. Bernevig, and T. L. Hughes, Phys. Rev. B **96**, 245115 (2017).
[10] F. Schindler, A. M. Cook, M. G. Vergniory, Z. Wang, S. S. P. Parkin, B. A. Bernevig, and T. Neupert, Sci. Adv. **4**, eaat0346 (2018).
[11] B. Bradlyn, L. Elcoro, J. Cano, M. Vergniory, Z. Wang, C. Felser, M. I. Aroyo, and B. A. Bernevig, Nature (London) **547**, 298 (2017).
[12] F. Schindler, Z. Wang, M. G. Vergniory, A. M. Cook, A. Murani, S. Sengupta, A. Y. Kasumov, R. Deblock, S. Jeon, I.

Drozdov, H. Bouchiat, S. Guéron, A. Yazdani, B. A. Bernevig, and T. Neupert, Nat. Phys. **14**, 918 (2018).
[13] C. Yue, Y. Xu, Z. Song, H. Weng, Y.-M. Lu, C. Fang, and X. Dai, Nat. Phys. **15**, 577 (2019).
[14] Z. Wang, B. J. Wieder, J. Li, B. Yan, and B. A. Bernevig, Phys. Rev. Lett. **123**, 186401 (2019).
[15] T. Zhang, Y. Jiang, Z. Song, H. Huang, Y. He, Z. Fang, H. Weng, and C. Fang, Nature (London) **566**, 475 (2019).
[16] M. Vergniory, L. Elcoro, C. Felser, N. Regnault, B. A. Bernevig, and Z. Wang, Nature (London) **566**, 480 (2019).
[17] F. Tang, H. C. Po, A. Vishwanath, and X. Wan, Nat. Phys. **15**, 470 (2019).
[18] F. Tang, H. C. Po, A. Vishwanath, and X. Wan, Nature (London) **566**, 486 (2019).
[19] Y. Xu, Z. Song, Z. Wang, H. Weng, and X. Dai, Phys. Rev. Lett. **122**, 256402 (2019).
[20] X.-L. Sheng, C. Chen, H. Liu, Z. Chen, Z.-M. Yu, Y. X. Zhao, and S. A. Yang, Phys. Rev. Lett. **123**, 256402 (2019).
[21] B. Liu, G. Zhao, Z. Liu, and Z. F. Wang, Nano Lett. **19**, 6492 (2019).
[22] E. Lee, R. Kim, J. Ahn, and B.-J. Yang, npj Quantum Mater. **5**, 1 (2020).

[23] C. Chen, W. Wu, Z.-M. Yu, Z. Chen, Y. X. Zhao, X.-L. Sheng, and S. A. Yang, Phys. Rev. B **104**, 085205 (2021).

[24] M. J. Park, Y. Kim, G. Y. Cho, and S. B. Lee, Phys. Rev. Lett. **123**, 216803 (2019).

[25] B. Liu, L. Xian, H. Mu, G. Zhao, Z. Liu, A. Rubio, and Z. F. Wang, Phys. Rev. Lett. **126**, 066401 (2021).

[26] M. Ezawa, Phys. Rev. B **98**, 045125 (2018).

[27] M. Hitomi, T. Kawakami, and M. Koshino, Phys. Rev. B **104**, 125302 (2021).

[28] C. Chen, Z. Song, J.-Z. Zhao, Z. Chen, Z.-M. Yu, X.-L. Sheng, and S. A. Yang, Phys. Rev. Lett. **125**, 056402 (2020).

[29] S. K. Radha and W. R. L. Lambrecht, Phys. Rev. B **102**, 115104 (2020).

[30] H. Huang and F. Liu, Natl. Sci. Rev. **2021**, nwab170 (2021).

[31] S. Qian, C.-C. Liu, and Y. Yao, Phys. Rev. B **104**, 245427 (2021).

[32] M. Pan, D. Li, J. Fan, and H. Huang, npj Comput. Mater. **8**, 1 (2022).

[33] Y. X. Zhao and Y. Lu, Phys. Rev. Lett. **118**, 056401 (2017).

[34] M. Nakahara, *Geometry, Topology and Physics*, 2nd ed. (Institute of Physics, Bristol, 2003).

[35] Z. Song, Z. Wang, W. Shi, G. Li, C. Fang, and B. A. Bernevig, Phys. Rev. Lett. **123**, 036401 (2019).

[36] J. Ahn, S. Park, and B.-J. Yang, Phys. Rev. X **9**, 021013 (2019).

[37] K. Wang, J.-X. Dai, L. B. Shao, S. A. Yang, and Y. X. Zhao, Phys. Rev. Lett. **125**, 126403 (2020).

[38] R. H. Baughman, H. Eckhardt, and M. Kertesz, J. Chem. Phys. **87**, 6687 (1987).

[39] D. Malko, C. Neiss, F. Viñes, and A. Görling, Phys. Rev. Lett. **108**, 086804 (2012).

[40] G. Li, Y. Li, H. Liu, Y. Guo, Y. Li, and D. Zhu, Chem. Commun. **46**, 3256 (2010).

[41] Z. Chen, C. Molina-Jirón, S. Klyatskaya, F. Klappenberger, and M. Ruben, Ann. Phys. **529**, 1700056 (2017).

[42] Z. Jia, Y. Li, Z. Zuo, H. Liu, C. Huang, and Y. Li, Acc. Chem. Res. **50**, 2470 (2017).

[43] X. Gao, H. Liu, D. Wang, and J. Zhang, Chem. Soc. Rev. **48**, 908 (2019).

[44] S. Jana, A. Bandyopadhyay, and D. Jana, Phys. Chem. Chem. Phys. **21**, 13795 (2019).

[45] B. G. Kim and H. J. Choi, Phys. Rev. B **86**, 115435 (2012).

[46] A. Bandyopadhyay and D. Jana, Rep. Prog. Phys. **83**, 056501 (2020).

[47] S. Jana, A. Bandyopadhyay, S. Datta, D. Bhattacharya, and D. Jana, J. Phys.: Condens. Matter **34**, 053001 (2022).

[48] W. A. Benalcazar, T. Li, and T. L. Hughes, Phys. Rev. B **99**, 245151 (2019).

[49] J. M. B. Lopes dos Santos, N. M. R. Peres, and A. H. Castro Neto, Phys. Rev. Lett. **99**, 256802 (2007).

[50] O. Leenaerts, B. Partoens, and F. M. Peeters, Appl. Phys. Lett. **103**, 013105 (2013).

[51] J. C. Slater and G. F. Koster, Phys. Rev. **94**, 1498 (1954).

[52] C. Chen, X.-T. Zeng, Z. Chen, Y. X. Zhao, X.-L. Sheng, and S. A. Yang, Phys. Rev. Lett. **128**, 026405 (2022).

[53] J. Ahn, D. Kim, Y. Kim, and B.-J. Yang, Phys. Rev. Lett. **121**, 106403 (2018).

[54] L. Zou, H. C. Po, A. Vishwanath, and T. Senthil, Phys. Rev. B **98**, 085435 (2018).

[55] S. Imhof, C. Berger, F. Bayer, J. Brehm, L. W. Molenkamp, T. Kiessling, F. Schindler, C. H. Lee, M. Greiter, T. Neupert, and R. Thomale, Nat. Phys. **14**, 925 (2018).

[56] G. Ma, M. Xiao, and C. T. Chan, Nat. Rev. Phys. **1**, 281 (2019).

[57] H. Xue, Y. Ge, H.-X. Sun, Q. Wang, D. Jia, Y.-J. Guan, S.-Q. Yuan, Y. Chong, and B. Zhang, Nat. Commun. **11**, 2442 (2020).

[58] H. Xue, Y. Yang, F. Gao, Y. Chong, and B. Zhang, Nat. Mater. **18**, 108 (2019).

[59] T. Ozawa, H. M. Price, A. Amo, N. Goldman, M. Hafezi, L. Lu, M. C. Rechtsman, D. Schuster, J. Simon, O. Zilberberg, and I. Carusotto, Rev. Mod. Phys. **91**, 015006 (2019).

[60] S. Mittal, V. V. Orre, G. Zhu, M. A. Gorlach, A. Poddubny, and M. Hafezi, Nat. Photonics **13**, 692 (2019).

[61] E. Prodan and C. Prodan, Phys. Rev. Lett. **103**, 248101 (2009).

[62] J. Dalibard, F. Gerbier, G. Juzeliūnas, and P. Öhberg, Rev. Mod. Phys. **83**, 1523 (2011).

[63] C. L. Kane and E. J. Mele, Phys. Rev. Lett. **95**, 226801 (2005).

[64] G. Kresse and J. Hafner, Phys. Rev. B **49**, 14251 (1994).

[65] G. Kresse and J. Furthmüller, Phys. Rev. B **54**, 11169 (1996).

[66] P. E. Blöchl, Phys. Rev. B **50**, 17953 (1994).

[67] J. P. Perdew, K. Burke, and M. Ernzerhof, Phys. Rev. Lett. **77**, 3865 (1996).

[68] S. Grimme, J. Antony, S. Ehrlich, and H. Krieg, J. Chem. Phys. **132**, 154104 (2010).

[69] S. Grimme, S. Ehrlich, and L. Goerigk, J. Comput. Chem. **32**, 1456 (2011).

[70] P. Moon and M. Koshino, Phys. Rev. B **87**, 205404 (2013).

[71] Y.-Q. Wang and J. E. Moore, Phys. Rev. B **99**, 155102 (2019).